Spatially aliased seismic reflection data

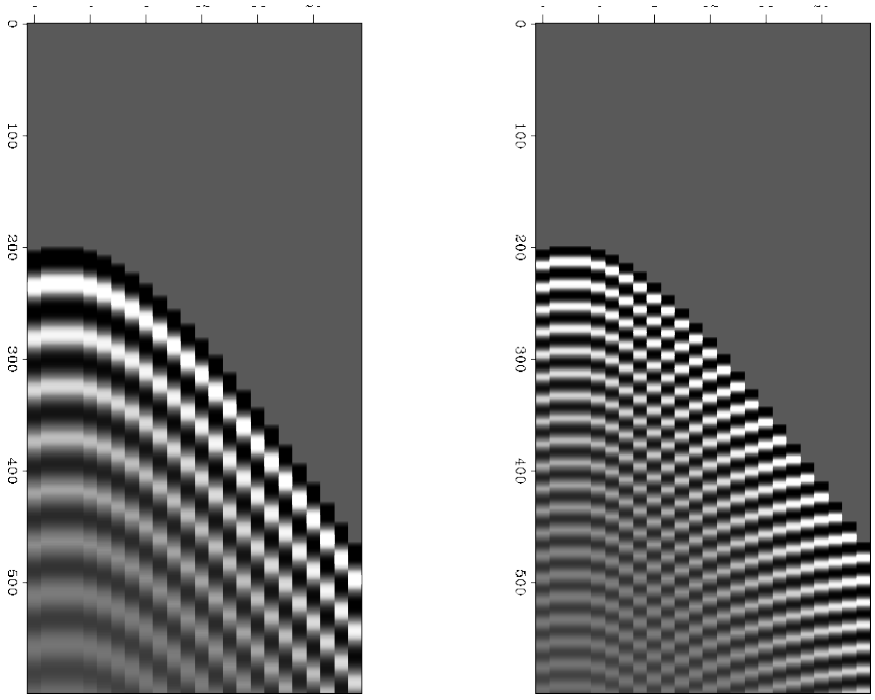

http://sepwww.stanford.edu/sep/prof/iei/omk/paper_html/node13.html

Figure 6.4-4: Relation between frequency amplitude spectrum and discrete Fourier transform (DFT).

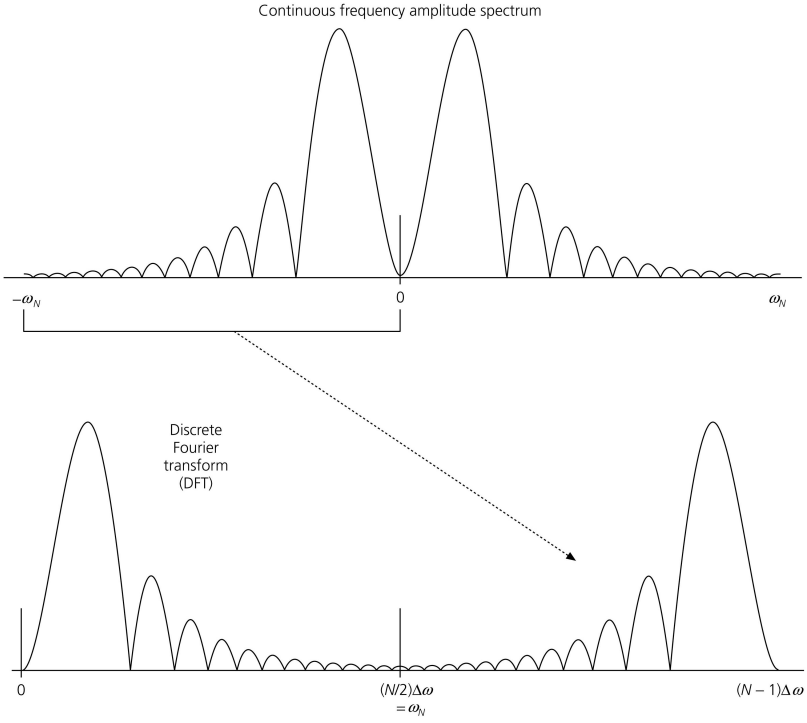

Splitting Patterns Suggest Long Fault Rupture

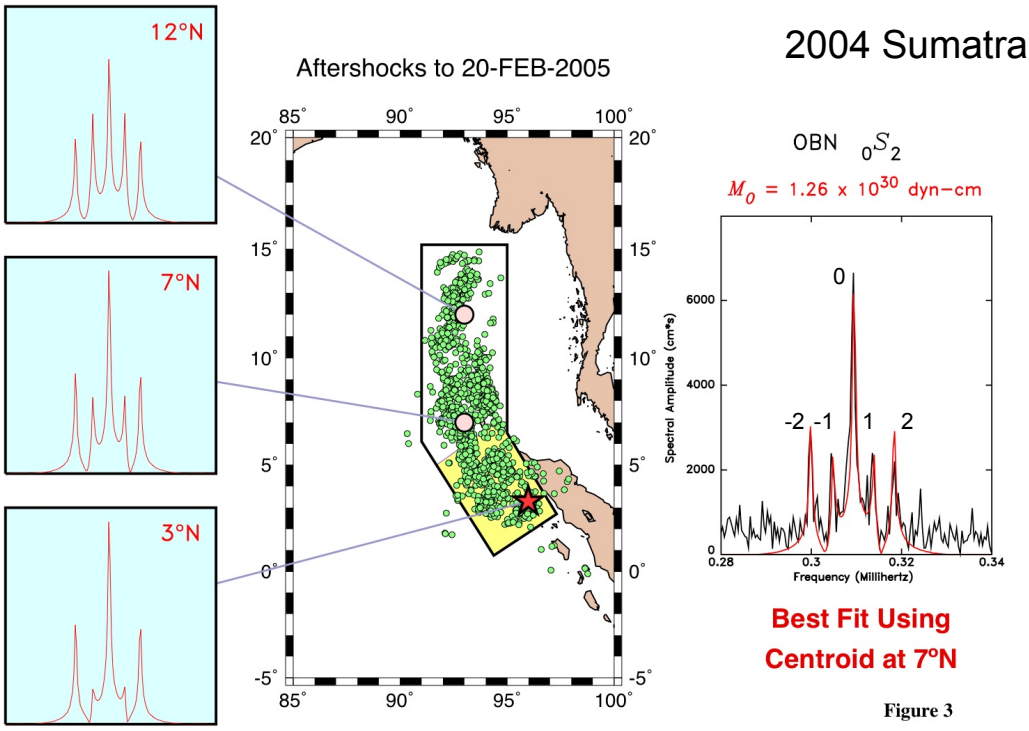

Figure 3

Stein & Okal, 2007

Figure 6.2-4: Amplitude spectra of a vertical-component seismogram from the great 1994 Bolivian earthquake.

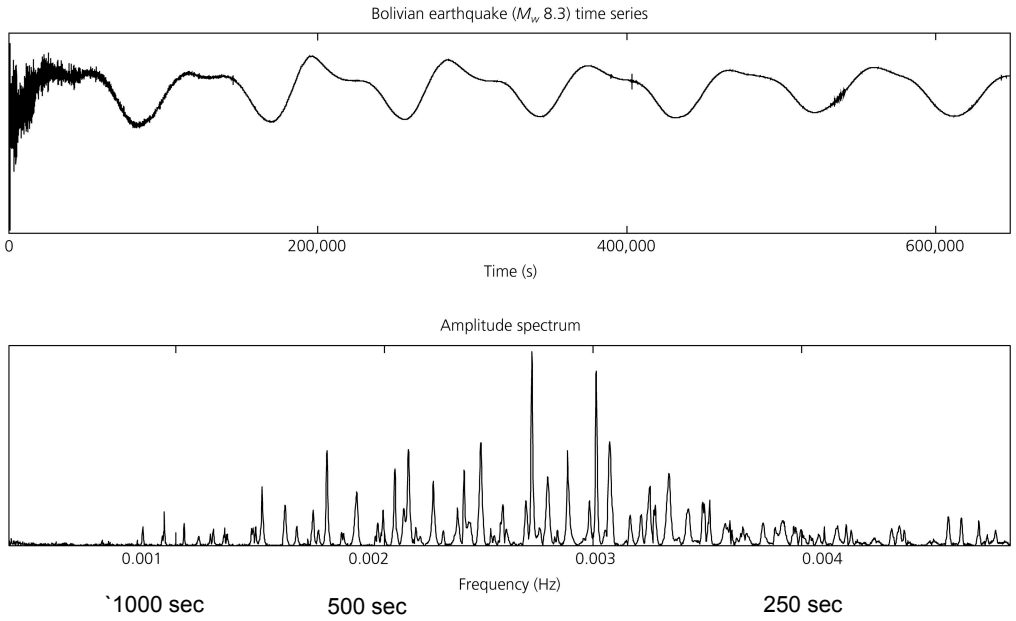

`1000 sec 500 sec 250 sec

Figure 6.4-5: Example of a time domain convolution.

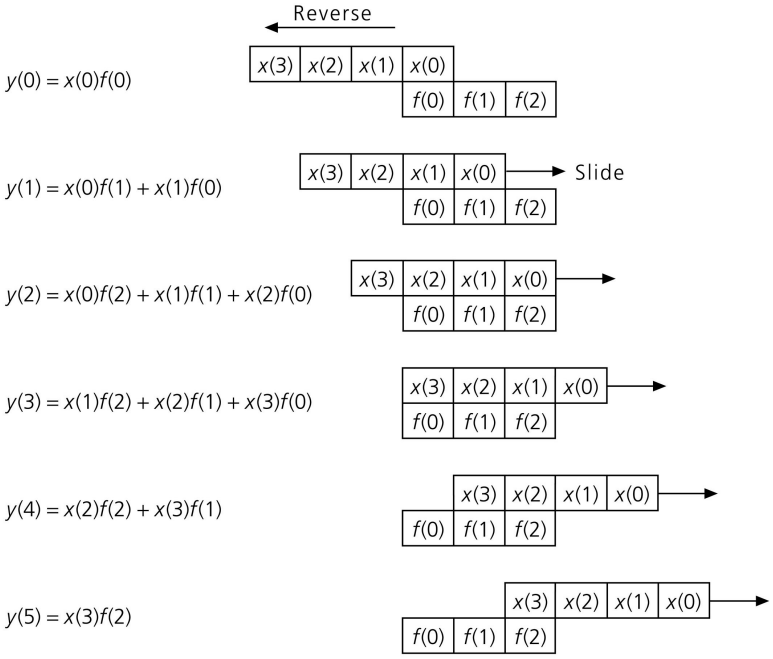

Precision vs accuracy

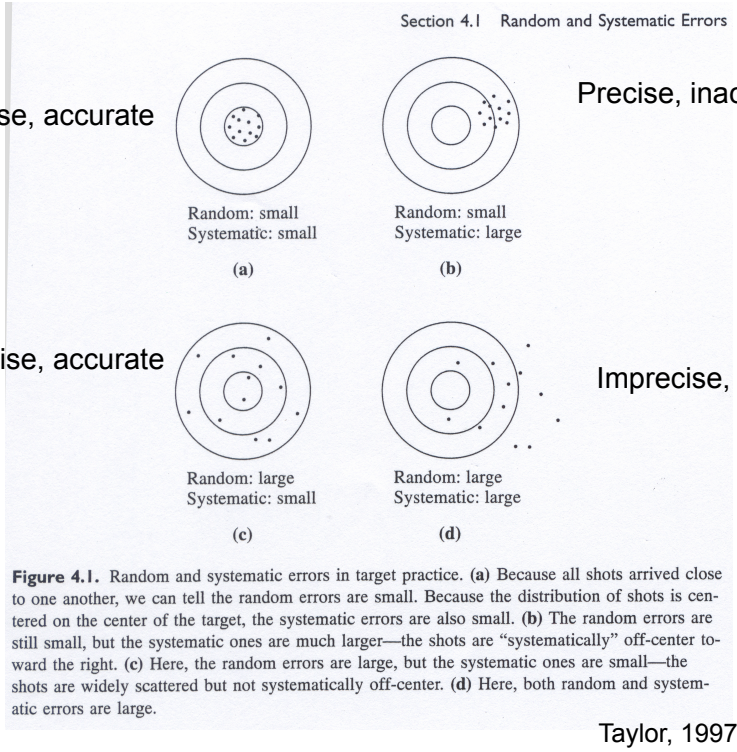

Figure 4.1. Random and systematic errors in target practice. **(a)** Because all shots arrived close to one another, we can tell the random errors are small. Because the distribution of shots is centered on the center of the target, the systematic errors are also small. **(b)** The random errors are still small, but the systematic ones are much larger—the shots are "systematically" off-center toward the right. **(c)** Here, the random errors are large, but the systematic ones are small—the shots are widely scattered but not systematically off-center. **(d)** Here, both random and systematic errors are large.

Precise, accurate

Precise, inaccurate

Imprecise, accurate

Imprecise, inaccurate

Taylor, 1997

Precision vs accuracy

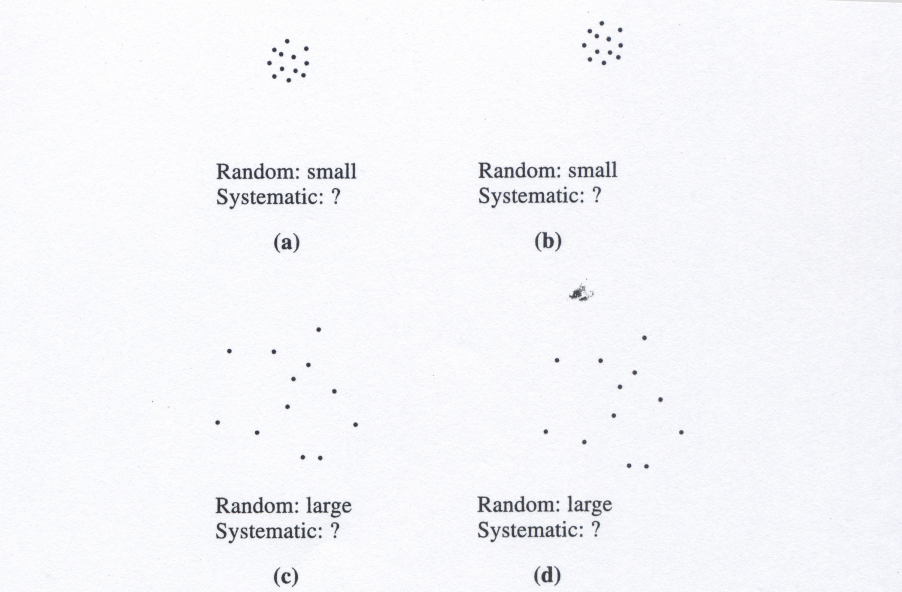

Figure 4.2. The same experiment as in Figure 4.1 redrawn without showing the position of the target. This situation corresponds closely to the one in most real experiments, in which we do not know the true value of the quantity being measured. Here, we can still assess the random errors easily but cannot tell anything about the systematic ones.

Taylor, 1997

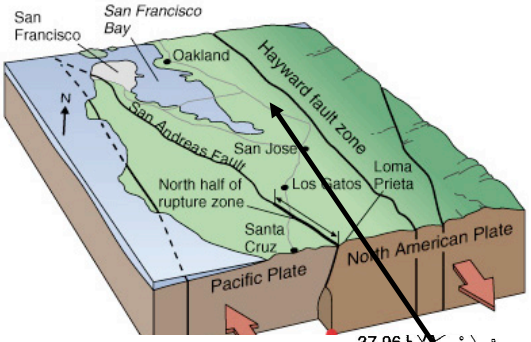

location of Hayward Fault earthquakes

1984-1989

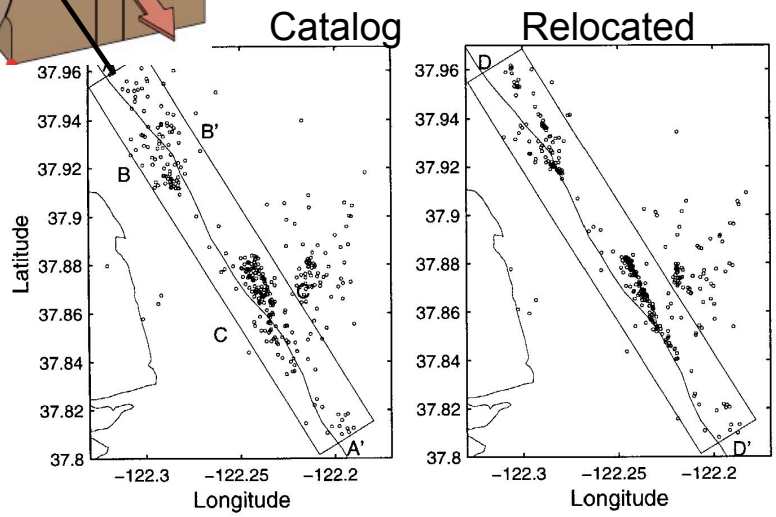

Waldhauser F. and W.L. Ellsworth, BSSA, 2000.

Some of the (generally small) discrepancies between plate motion rates found from space geodesy & from magnetic anomalies result from errors in the paleomagnetic timescale

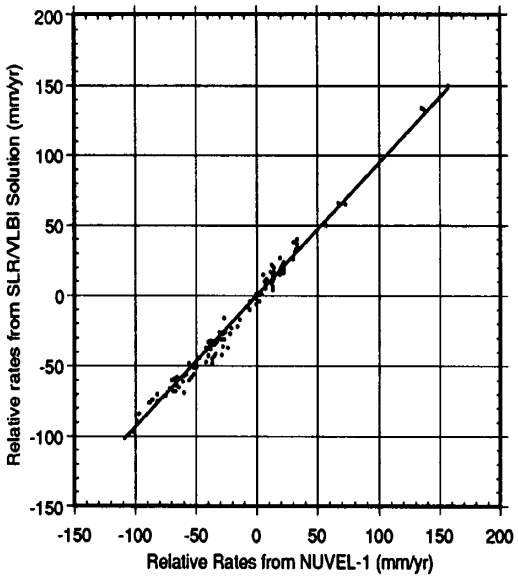

Robbins et al., 1993

USING KNOWN HISTORY OF EARTH'S MAGNETIC FIELD, ANOMALIES CAN BE COMPUTED AND COMPARED TO THOSE OBSERVED TO DETERMINE SPREADING RATES

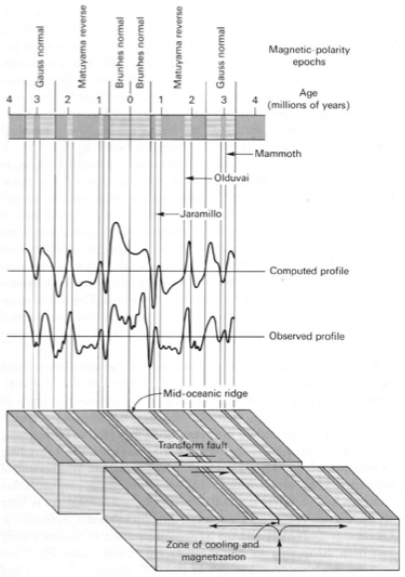

Uyeda, 1978

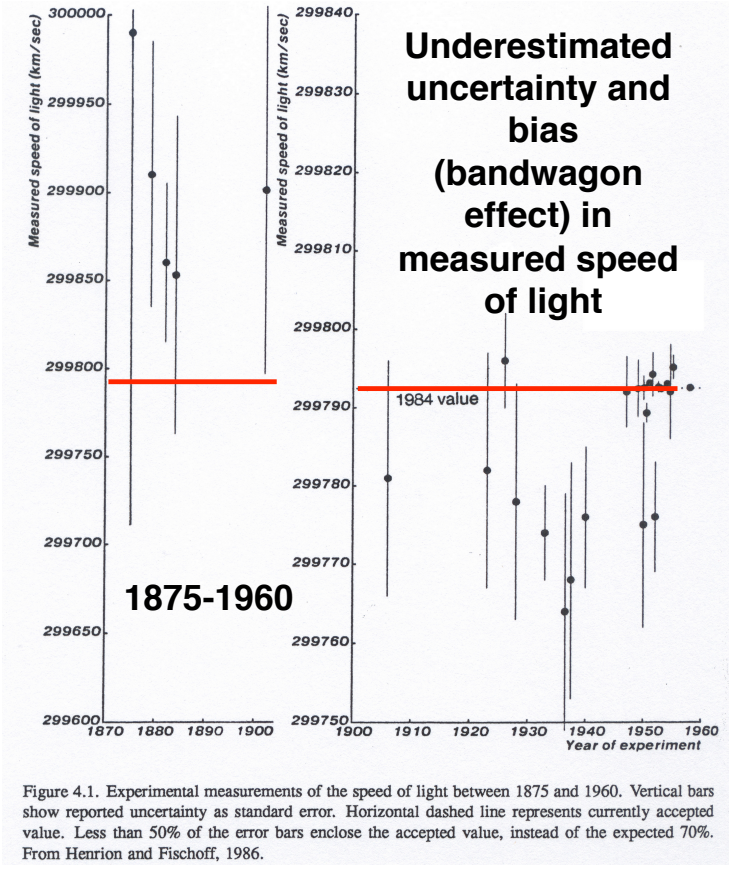

Figure 4.1. Experimental measurements of the speed of light between 1875 and 1960. Vertical bars show reported uncertainty as standard error. Horizontal dashed line represents currently accepted value. Less than 50% of the error bars enclose the accepted value, instead of the expected 70%. From Henrion and Fischoff, 1986.

Uncertainties are hard to assess and generally underestimated

Systematic errors often exceed measurement errors

Gaussian distribution

Figure 6.5-1: Gaussian distribution.

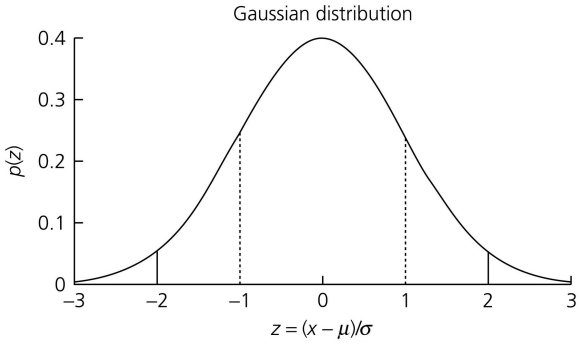

Figure 6.5-2: Results of drawing N samples from a Gaussian parent distribution.

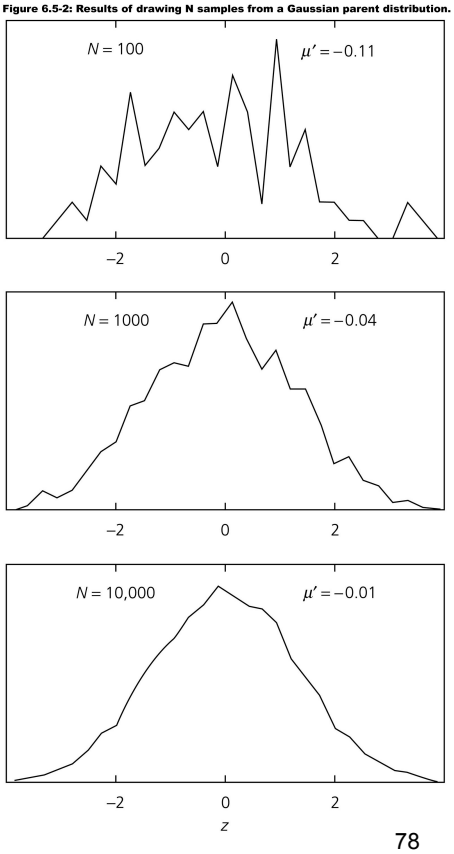

Stein &Wysession, 2003

MISSING CARBON SINK?

Atmospheric increase	
=	
Emissions from fossil fuels	3.2 (±0.2)
+	=
Net emissions from changes in land use	6.3 (±0.4)
-	+
Oceanic uptake	2.2 (±0.8)
-	-
Missing carbon sink ←	2.4 (±0.7)
	-
	2.9 (±1.1) ←

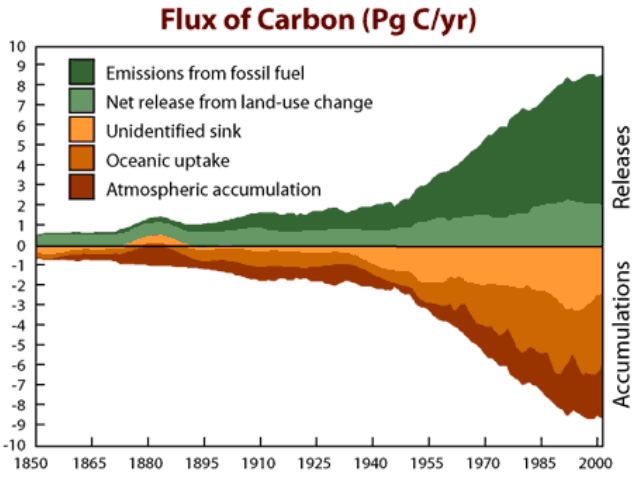

http://www.whrc.org/carbon/missingc.htm

PRECISION OF GEODETIC VELOCITY ESTIMATES

Depend on precision of each position and the time span of measurements

Rate v of motion of a monument that started at position x_1 and reaches x_2 in time T

$$v = (x_1 - x_2)/T$$

If position uncertainty is given by standard deviation σ

Rate uncertainty is

$$\sigma_v = 2^{1/2} \sigma / T$$

Thus rate precision improves, even if the data do not become more precise

Older geodetic data, for example that taken shortly after the 1906 San Francisco earthquake, can be of great value even if their errors are larger than those of more modern data.

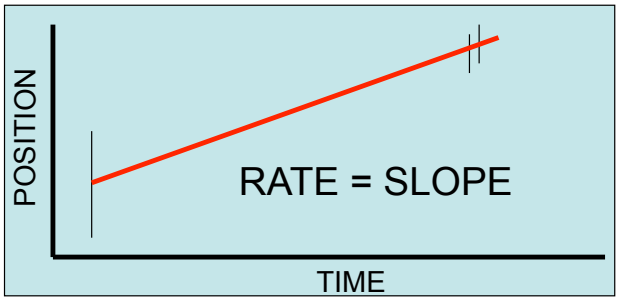

GPS VELOCITY ESTIMATES

Precision of velocity estimates depends on precision of site position & length of time

Velocity from a weighted least squares line fit to positions

Precision increases over time

Horizontal precision is better

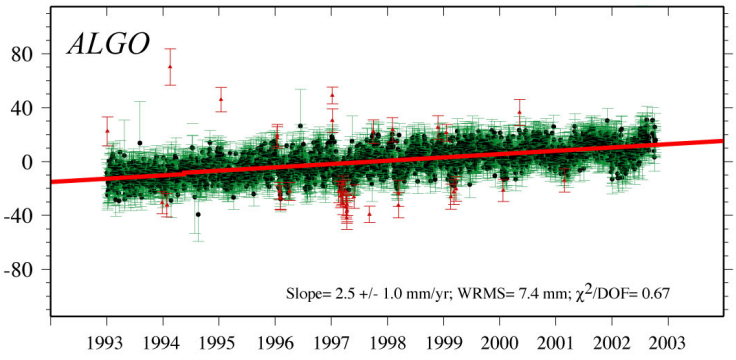

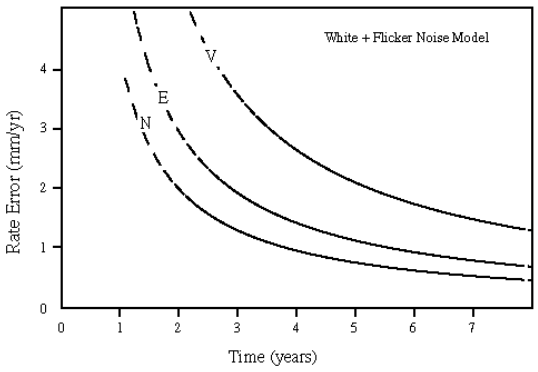

Sella et al., 2002

GPS velocity estimate uncertainty vs measurement timespan

Expect error proportional to 1/ Timespan

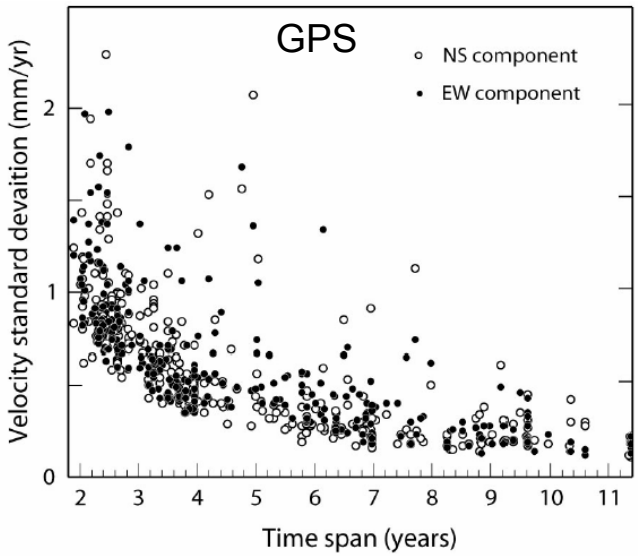

Figure 4. Velocity standard deviation as a function of measurement time span.

Calais et al, 2006

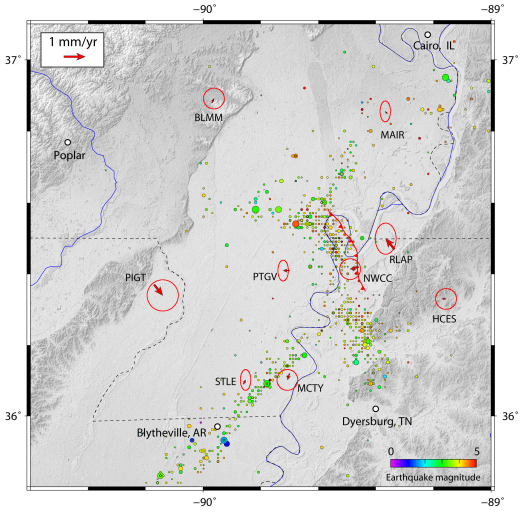

New Madrid:

- Residual velocities < 0.2 mm/yr
- Strain rate < 1.3×10^{-9} yr^{-1}
- uncertainties and residual velocities have decreased by at least a factor of 2 at all sites as time series lengthens
- Sites with the worse quality position time series such as RLAP also have the largest residuals

(more details in Calais and Stein, Science, 2009)

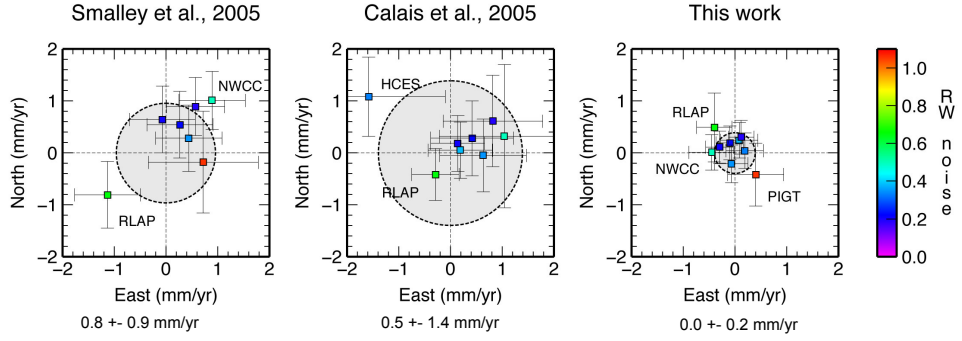

As New Madrid GPS data improve, primarily due to longer span of measurements, maximum possible motion keeps decreasing

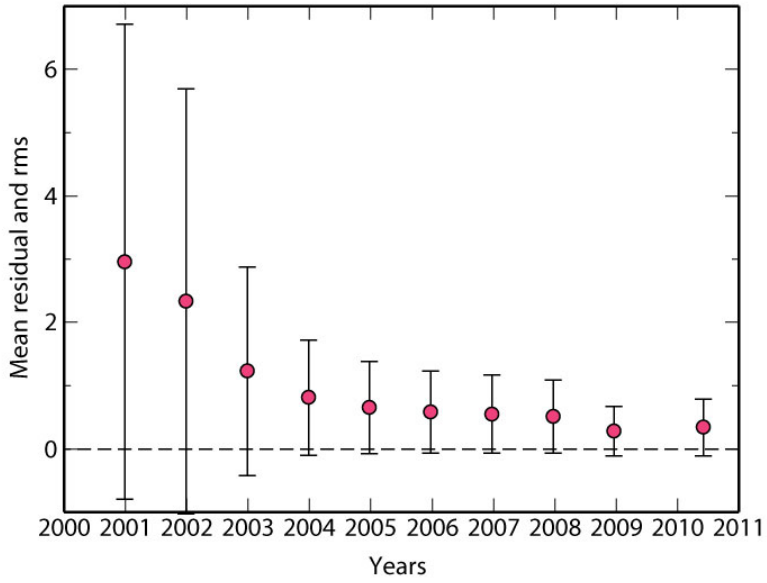

E. Calais

Figure 6.5-3: Example of stacking seismograms to enhance precursors to *SS*.

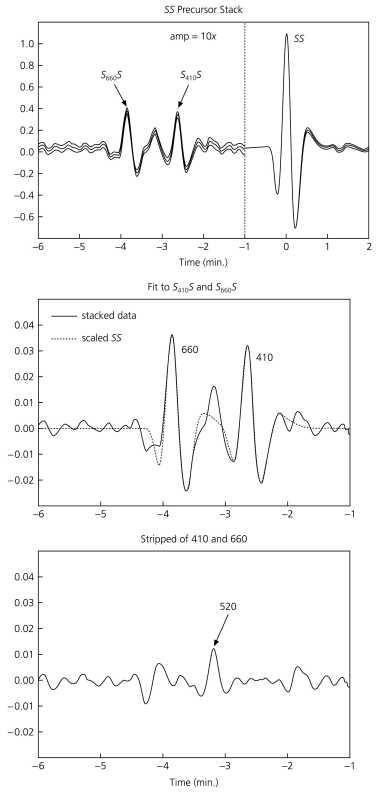

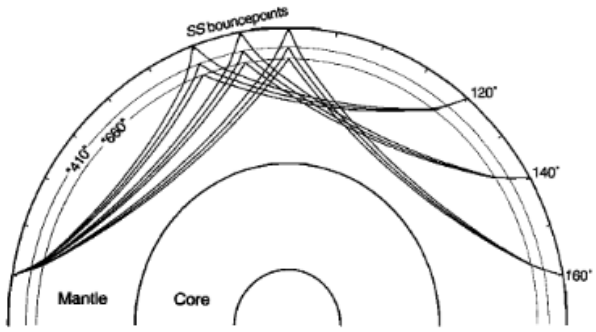

Figure 1. Ray paths of SS and the underside precursors $S410S$ and $S660S$ at source-receiver ranges of 120°, 140°, and 160°.

Figure 6.5-6: Stacking global seismograms to produce record sections.

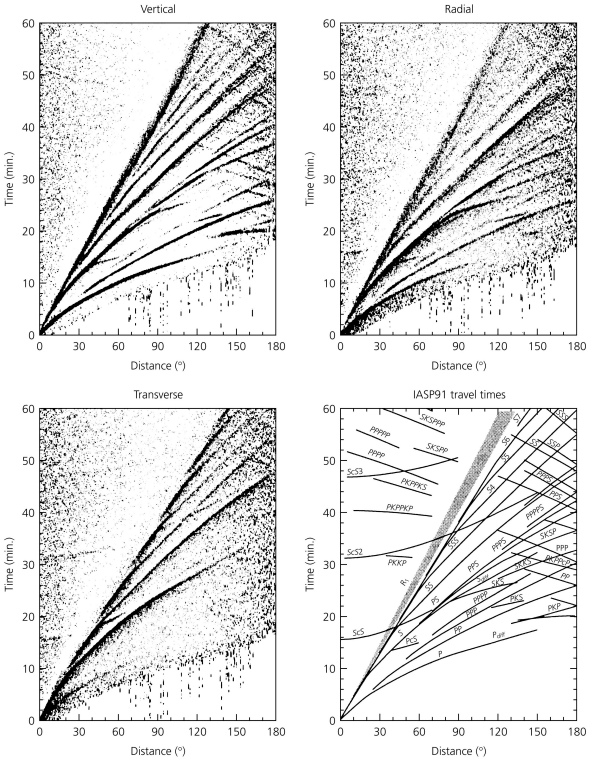

NORMAL MODES OF SPHERICAL EARTH

Displacement (traveling seismic waves) represented by 3-D sum in spherical coordinates of normal modes

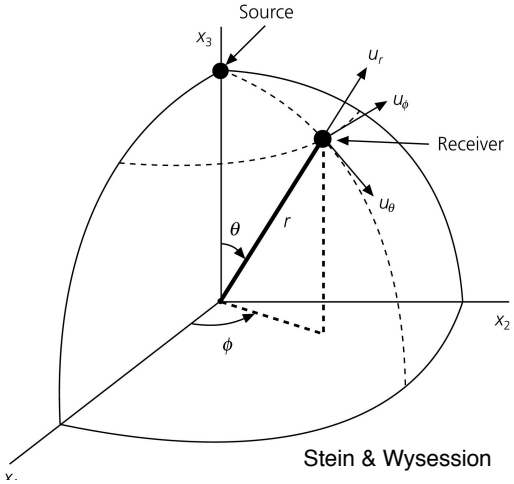

$$\mathbf{u}(r, \theta, \phi) = \sum_n \sum_l \sum_m {}_nA_l^m \; {}_ny_l(r) \; \mathbf{x}_l^m(\theta, \phi) \; e^{{}_n\omega_l^m t}$$

n, l, m - radial, angular, and azimuthal orders

${}_ny_l(r)$ - scalar radial eigenfunction

$\mathbf{x}_l^m(\theta, \phi)$ - vector surface eigenfunction

${}_nA_l^m$ - excitation amplitudes (weights for eigenfunctions) that depend on the seismic source.

Surface eigenfunctions are vector spherical harmonics: derivatives of $Y_{lm}(\theta, \phi)$

Figure 2.9-4: Examples of spherical harmonics.

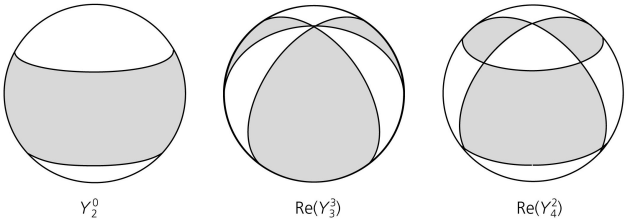

Figure 6.5-5: Example of stacking seismograms to enhance specific normal modes.

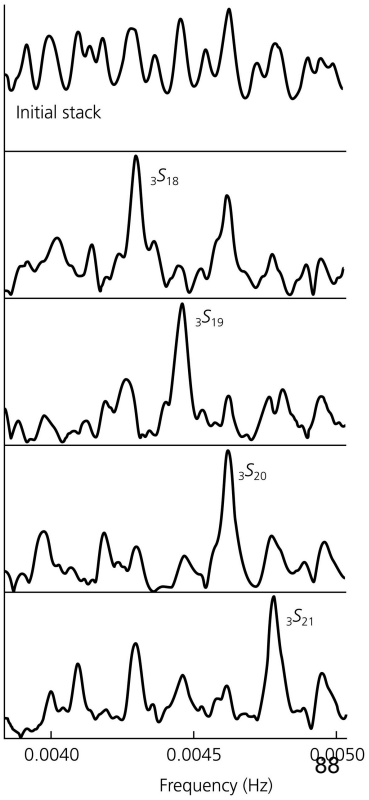

88

MAJO -- Matsushiro, Japan

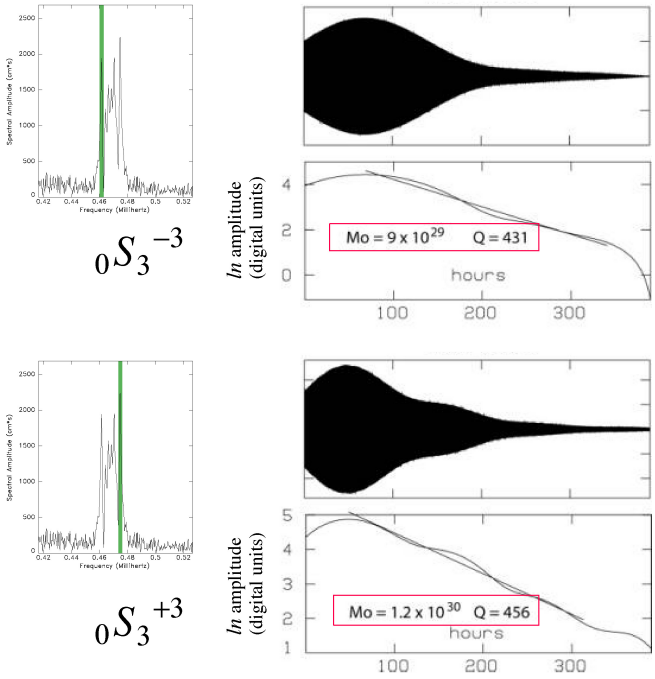

89

Okal & Stein, 2009

Figure 6.6-1: Diagram of a vertical seismograph.

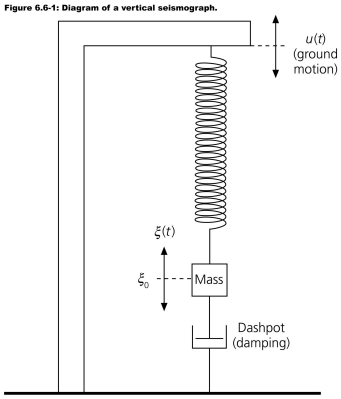

Figure 6.6-2: Amplitude response and phase delay for a pendulum seismometer

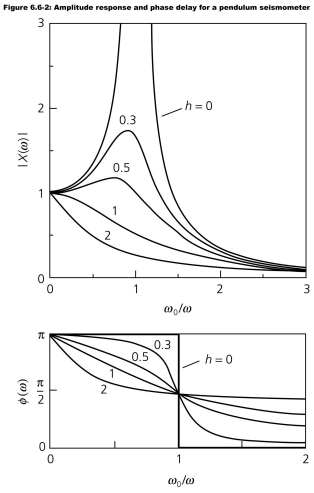

Figure 6.6-3: Demonstration of seismic noise on a broadband seismogram.

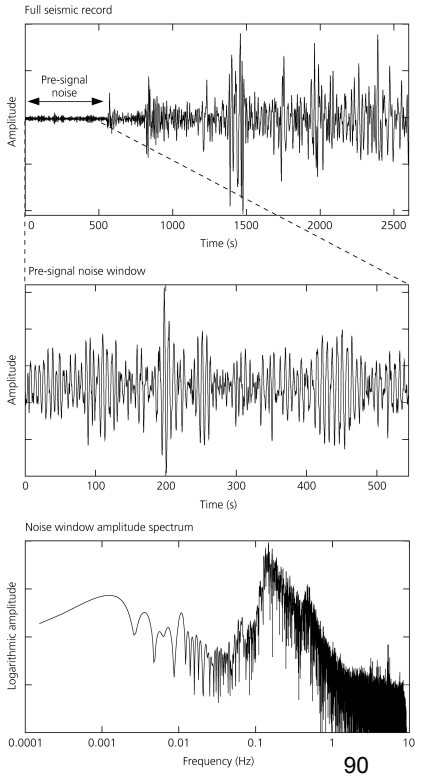

90

Wiechert horizontal seismometer, an entirely mechanical, seismometer, made in Gottingen (Germany) in 1904, and was in use in the Strasbourg seismic observatory between 1904 and 1968.

It is essentially an inverted pendulum, which records both components of horizontal motion on rolls of smoked paper. It weighs 1000 kg, and has a natural period of 8 seconds. Damping is provided by two air-pistons on the top of the instrument. The pendulum is centered by placing a series of small weights on top of the main mass.

http://sismordia.blogspot.com/2007/07/historical-seismometers-1-wiechert.html

Response of damped harmonic oscillator to harmonic wave peaked around natural frequency

Spectral resonance peaks:
Add a harmonic driving force to see how a damped harmonic oscillator responds:

$$\frac{d^2u}{dt^2} + \gamma \frac{du}{dt} + \omega_0^2 u = e^{i\omega t}$$

Choose a solution of the form: $u(t) = A(\omega)\, e^{i\phi(\omega)}\, e^{i\omega t}$

This gives: $A(\omega) = \dfrac{1}{\left[(\omega_0^2 - \omega^2)^2 + (\omega\gamma)^2\right]^{1/2}}$ $\phi = \tan^{-1}\left[\dfrac{-\gamma\omega}{\omega_0^2 - \omega^2}\right]$

Peak width proportional to 1/Q

Peak amplitude reduced

Normal modes, seismometers, buildings

Figure 3.7-13: Amplitude/phase of a forced, damped harmonic oscillator.

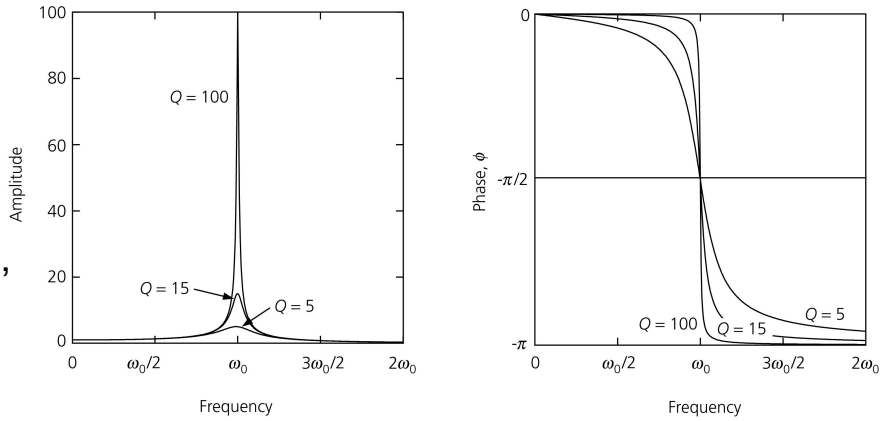

Figure 6.6-5: Illustration of an electromagnetic seismograph.

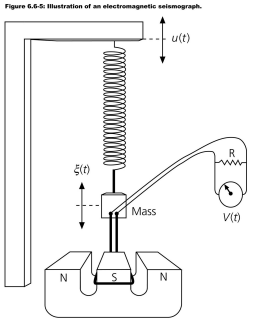

Figure 6.6-6: Coupling of the transducer of an electromagnetic seismograph to a galvanometer.

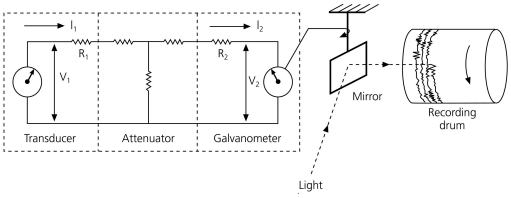

Figure 6.6-7: Responses of the components of an electromagnetic seismograph.

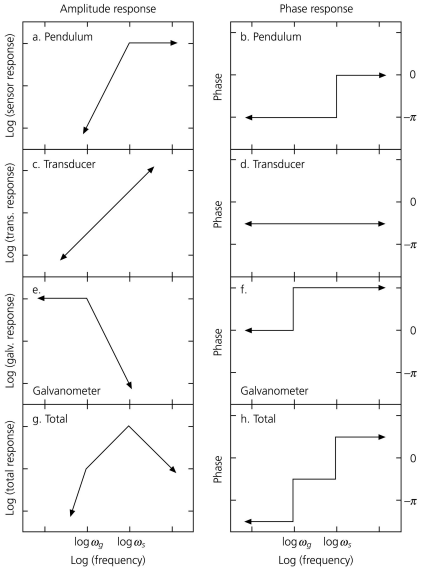

Figure 6.6-9: Sample WWSSN long-period vertical-component seismogram for one day.

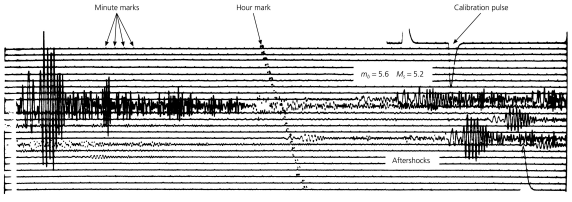

Figure 6.6-10: Diagram of the sensing and feedback electronics of an IDA gravimeter.

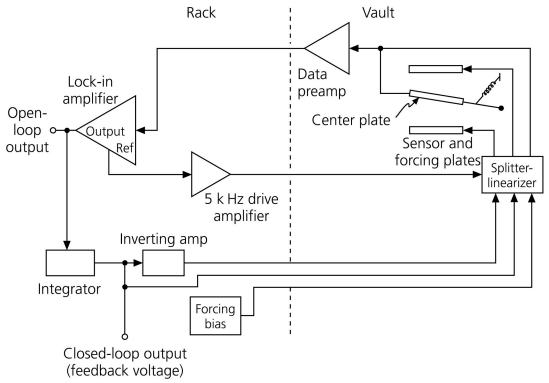

Figure 6.6-8: Instrument responses for several types of seismometers.

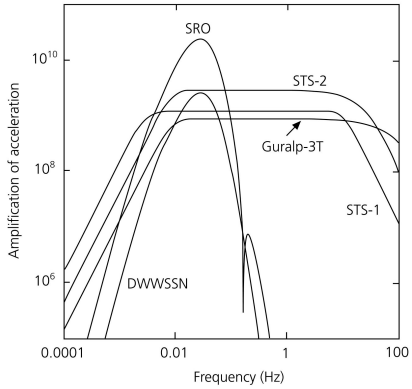

Figure 6.6-14: Relation between displacement, velocity, and acceleration in the time domain.

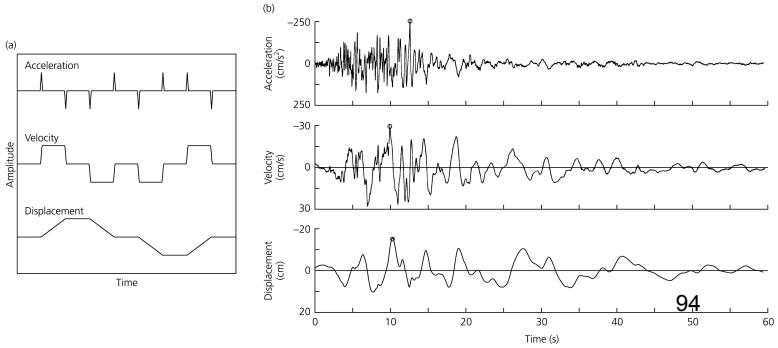

Figure 6.6-13: Example of a FIR filter and its effects on a seismogram.

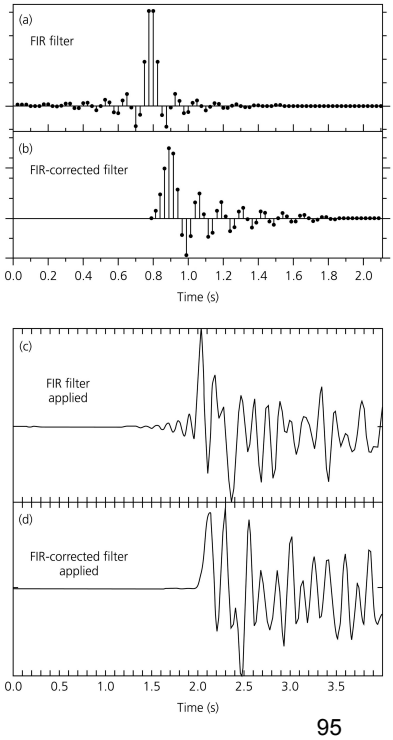

Figure 6.6-12: Diagram showing the analog-to-digital (ADC) process.

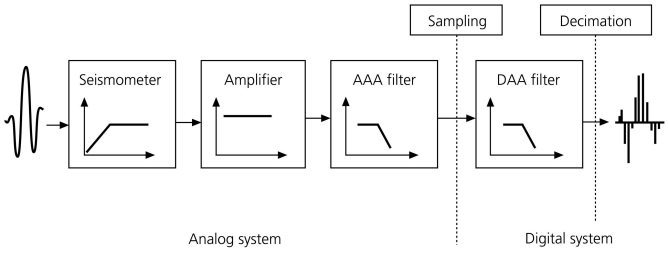

Spectrum of analog signal

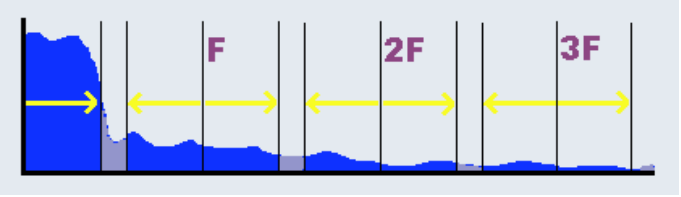

Oversample

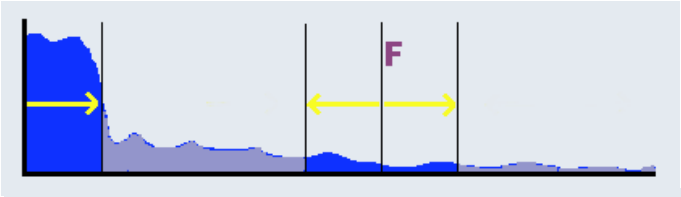

Analog filter

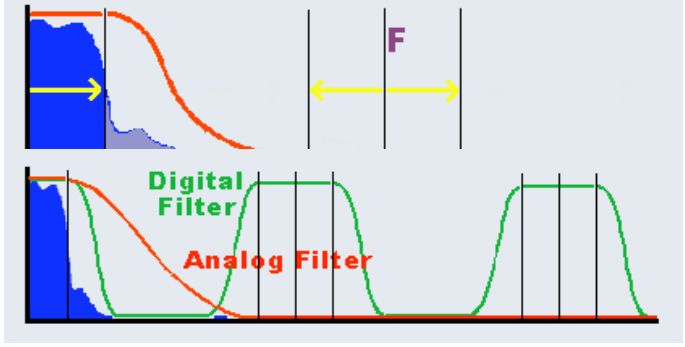

Digital filter

http://www.mstarlabs.com/dsp/antialiasing/antial.html

Figure 3.2-1: Ray paths for a layer over a halfspace.

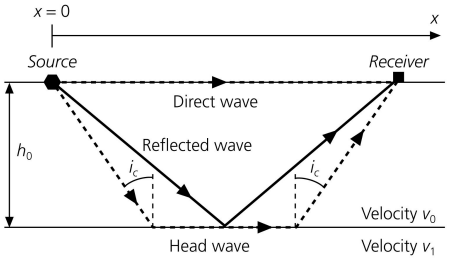

Figure 3.2-2: Travel time curve for rays in a layer over a halfspace.

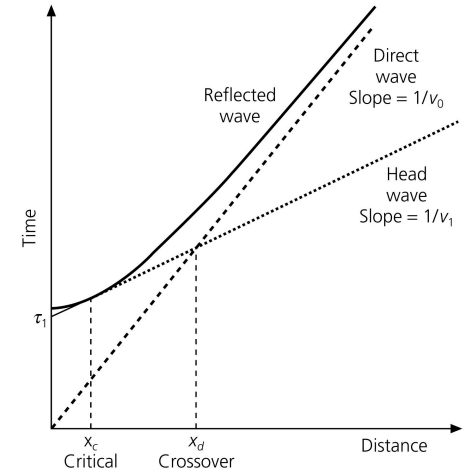

Figure 3.3-15: Diagram of the normal moveout correction.

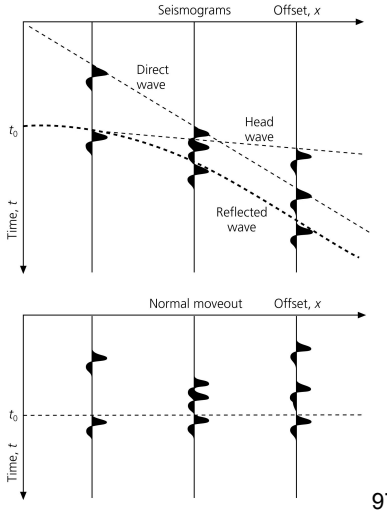

Figure 3.3-1: Hyperbolic travel time curve for an interface reflection.

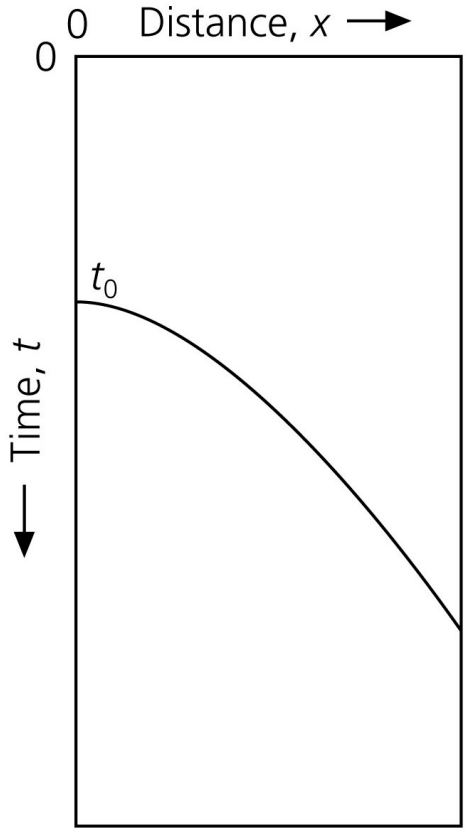

Offset:

$$T(x)^2 = x^2/\mathrm{v}_0^2 + 4h_0^2/\mathrm{v}_0^2 = x^2/\mathrm{v}_0^2 + t_0^2$$

Normal moveout:

$$T(x) - t_0 = (x^2/\mathrm{v}_0^2 + t_0^2)^{1/2} - t_0$$

Once the velocity is found, the layer thickness is given by the vertical travel time.

Figure 3.3-2: Cartoon demonstration of ray parameter.

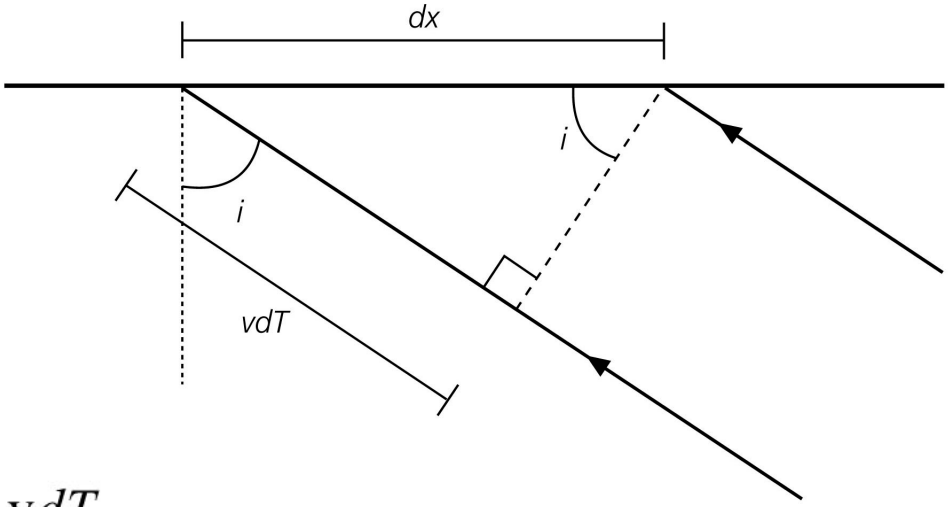

$$\sin i = \frac{\mathrm{v}dT}{dx}$$

$$p = \frac{\sin i}{\mathrm{v}} = 1/c_x = \frac{dT}{dx}$$

Total horizontal distance

$$x(p) = 2\sum_{j=0}^{n} x_j = 2\sum_{j=0}^{n} h_j \tan i_j$$

in a total time

$$T(p) = 2\sum_{j=0}^{n} \Delta T_j = 2\sum_{j=0}^{n} \frac{h_j}{\mathrm{v}_j \cos i_j}$$

For multiple layers,
multiple hyperbolas:

$$T(x)^2_{n+1} = x^2/\bar{\mathrm{V}}^2_n + t^2_n$$

where t_n is the vertical
2-way travel time:

$$t_n = 2\sum_{j=0}^{n} \Delta t_j = 2\sum_{j=0}^{n} (h_j/\mathrm{v}_j)$$

and

$$x = 2\sum_{j=0}^{n} x_j = 2\,\frac{\sin i_0}{\mathrm{v}_0} \sum_{j=0}^{n} \mathrm{v}_j^2 \Delta T_j \ .$$

Figure 3.3-3: Ray path through multilayered structure.